

Research Paper

Improved print quality in fused filament fabrication through localized dispensing of hot air around the deposited filament



Hardikkumar Prajapati¹, Swapnil S. Salvi¹, Darshan Ravoori, Momen Qasaimeh,
Ashfaq Adnan, Ankur Jain*

Mechanical and Aerospace Engineering Department, University of Texas at Arlington, Arlington, TX, USA

ARTICLE INFO

Keywords:
Additive manufacturing
Polymer extrusion
Temperature measurement
Infrared thermography
Filament adhesion

ABSTRACT

Bonding between polymer filaments deposited during Fused Filament Fabrication (FFF) is a critical process that determines the quality of the printed part. This process is governed by the temperature history of the deposited filament. In general, the longer the filament stays above glass transition temperature, the greater is the quality of bonding. This paper presents a technique to enhance FFF quality by localized dispensing of hot air from nozzles integrated with the main polymer-dispersing nozzle, thereby providing a hot micro-environment around the filament. The temperature field during this process is measured using infrared thermography. It is shown that under the correct process conditions, this approach results in significantly reduced heat transfer from the filament, thereby increasing the cool down time and improving the quality of bonding with the adjacent filaments. The improved thermal history of the filament due to hot air dispensing is shown to translate into increased neck size, leading to 35% increase in thermal conductivity, 19% increase in tensile strength and 145% increase in tensile toughness. Compared to other thermal techniques for improving the FFF process proposed in the past, the present approach provides a highly localized, *in situ* thermal enhancement of the local environment around the deposited filament, and integrates seamlessly with the filament-dispersing nozzle. It is expected that the technique described here may help improve the quality of FFF process and enable the printing of parts with improved thermal and mechanical properties.

1. Introduction

Polymer extrusion based additive manufacturing (AM) processes such as Fused Filament Fabrication (FFF) are being extensively used for rapid printing of functional parts and components capable of withstanding various forms of mechanical load [1]. In these processes, a polymer is heated above its glass transition temperature, extruded through a nozzle and deposited on a platform in the form of multiple filaments. Adhesion between neighboring roads occurs due to reptation of polymer chains across the road-to-road interface, which provides mechanical strength to the printed part. Good adhesion between adjacent roads is critical for ensuring good mechanical properties of the printed part [2,3].

The process of road-to-road adhesion is driven by polymer healing, which refers to molecular diffusion across the interface of two adjacent polymer filaments [4,5]. This well-studied process is primarily driven by

diffusion of polymer chains across the interface. The extent of healing, and hence adhesion, that occurs during the short cooling time of the filament is known to be strongly driven by the temperature history of the road-to-road interface. Theoretical modeling of the reptation of polymer chains across the interface [4,6] shows that the longer the interface remains above glass transition temperature, the greater is the degree of healing, and hence, the greater is the bond strength. While raising the filament deposition temperature will, in principle, result in greater time spent above glass transition, too large a deposition temperature may result in polymer degradation and surface defects. Instead, it is important to minimize heat loss from the dispensed filament into the surroundings in order to prolong the cooling curve.

Motivated by the connection between filament temperature and bond strength of the printed part, significant experimental and theoretical research has been carried out on understanding and optimizing the thermal environment around a dispensed filament. The key

* Correspondence to: 500 W First St, Rm 211, Arlington, TX 76019, USA.

E-mail address: jaina@uta.edu (A. Jain).

¹ Equal Contributors.

mechanisms responsible for the cooling of a deposited filament include thermal conduction to neighboring filaments and the material on which the filament is deposited, as well as heat loss to the surrounding air [2,3, 7]. The build platform is typically heated to a high temperature in order to suppress conduction heat losses. Heat transfer modeling has been carried out to understand these heat transfer mechanisms responsible for the cooling curve of the filament. One- [6] and two-dimensional [8] thermal models have been developed for the cooling of the filament due to convection into its surroundings. Thermal conduction models have been developed for heat transfer from the filament in the stand-off gap prior to deposition [9] and onto the build platform after deposition [2]. Numerical models have been developed to predict temperature evolution during the printing of a complete part [3,10,11] and thus predict regions of good and poor adhesion [3]. On the experimental side, infrared (IR) thermography has been extensively used for measuring and characterizing the evolution of the temperature field [2,7,12–16], including at the liquefier exit [17] and in the standoff gap [9]. Measurements of the interface temperature between two filaments have shown that the interface temperature stays above glass transition temperature only for a short amount of time [7], which highlights the key challenge of prolonging this time in order to enhance the degree of healing and thus improve bond strength. While post-process thermal annealing methods have been shown to result in improved filament adhesion, leading to enhanced thermal [18] and mechanical properties [19], these methods require large annealing time and may result in warping.

A heated build environment is commonly used in polymer 3D printing to control the temperature of the air around the filament being deposited. This may help minimize thermal warping and loss of dimensional accuracy of the printed part. However, heating up a large volume of air within the 3D printing equipment may be expensive and time-consuming, and there are usually limitations on how high a temperature can be maintained. It may be more desirable to heat up the air in the immediate vicinity of the filament being deposited. By applying heat only in the region where it is needed, this approach may be more scalable, and may be used to maintain a very high temperature around the deposition site without subjecting the entire part to thermal stress. This may help minimize loss of dimensional accuracy.

Towards the goal of *in situ* control of the local thermal environment around the filament, heat from an external source of energy has been directed to the filament deposition site in order to keep the filament warm. Examples include infrared [20,21], laser [22], and microwave [23] heating. A heated metal element rastering along with the dispensing nozzle has been used for *in situ* filament heating in order to improve bond strength [16]. An inverted 3D printing process has been proposed, where the lower density of hot air is used to maintain a local high temperature environment around the rastering nozzle [24]. It is important that such thermal enhancement approaches to improve the thermal environment around the filament be local and as less disruptive to the printing process as possible.

Only limited literature is available on the use of hot air flow for localized heating during FFF. Partain [25] has described pre-deposition heating of the roads using hot air from a welding machine. However, the lack of quantitative temperature measurement in this work makes it difficult to fully understand the impact of such heating on temperature history at the road-to-road interface, and subsequently on road-to-road adhesion. Further, Partain did not find any improvement in mechanical strength of parts printed with hot air compared to baseline [25], which may have been because only pre-deposition heating was provided, whereas the extent of road-to-road adhesion is governed primarily by temperature history of the interface after deposition [7]. A hot air jet has also been used for post-process polishing of a 3D printed polymer part, with the goal of improving surface finish [26], although this work did not investigate *in situ* use of the hot air jet during the printing process.

In contrast with much of this past work that utilizes a large, external

energy source for heating, this paper presents a localized, *in situ* technique for controlling the thermal environment around a deposited filament using a hot air supply. Hot air at a desired temperature and flow rate is supplied from air nozzles that are integrated to move along with the filament-dispensing nozzle. The hot air impinges just before and after filament deposition and provides a warm environment around the filament that helps suppress the rate of cooling of the filament. This hypothesis is investigated in detail through infrared thermography based measurement of the temperature field during the FFF process. The resulting impact on void fraction and thermal/mechanical properties is investigated.

2. Experimental setup

2.1. Additive manufacturing platform

An open source Anet A8 3D printer with A-1284 controller board is used in printing and thermal visualization experiments. The samples for mechanical and thermal properties measurement are also printed on the same machine. The Computer-Aided Design (CAD) model of the sample geometry is imported into Simplify3D slicing software and converted to G-code. Process parameter such as layer height (0.4 mm), infill pattern (0°/0°), print speed (2000 and 3600 mm/min), bed temperature (110 °C) and nozzle temperature (230 °C) are specified in the slicing software. Acrylonitrile Butadiene Styrene (ABS) filament of black color and 1.75 mm diameter (Tronxy Ltd., Shenzhen, China) is used for all experiments, including measurement of the thermal field during printing, and printing of samples for thermal and mechanical properties measurement. Glass transition temperature of ABS is around 105 °C. Filament nozzle diameter is 0.4 mm. Before connecting the hot air supply described in Section 2.2, the build platform is leveled using a standard method. Points located at four corners and at the center are considered for leveling. The nozzle is moved to these points one-by-one and set to a *z* value of zero. The leveling screws are tightened or loosened as needed to make sure that a single sheet of paper passes between the nozzle and build platform with minimum resistance.

2.2. Hot air supply

A hot air supply manifold is integrated with the filament heater barrel. Fig. 1(a) and 1(b) show a schematic and a picture of the hot air supply manifold. Prior to entering the air supply manifold, standard laboratory air supply is heated up in an air heating section, from where, the air flows into the hot air supply manifold, and finally through the air nozzles on to the build platform. Fig. 2(a) and (b) shows a schematic and a picture of the entire hot air supply circuit, including the air preheating section and hot air supply manifold. Fig. 3 shows a schematic of the printing process in order to define the coordinate axes as well as print and build directions. The hot air supply manifold is manufactured separately and integrated to raster together with the filament nozzle barrel. The air supply manifold comprises brass elbow joints at the two ends for hot air entering from the air heating section, which is then directed to six nozzles of diameter 1 mm each. A 5 mm diameter internal hole is drilled in the hot air supply manifold to create the internal flow path. Three holes with M6 thread are drilled along the flow direction to accommodate six nozzles that discharge hot air over the build platform. Three nozzles are located on each side of the filament nozzle, so that one set of nozzles traveling ahead of the filament nozzle heat up the build platform prior to filament deposition, while the other set of nozzles traveling behind the filament nozzle provides continued heat to keep the filament from cooling too fast after deposition. The distance between two air nozzles is 9.8 mm and the first air nozzle is 20.4 mm from the filament nozzle. The clearance between the air nozzles and build platform is around 3.7 mm.

The hot air supply manifold has a threaded M6 hole at the center, the axis of which coincides with the filament barrel axis. Once placed on the

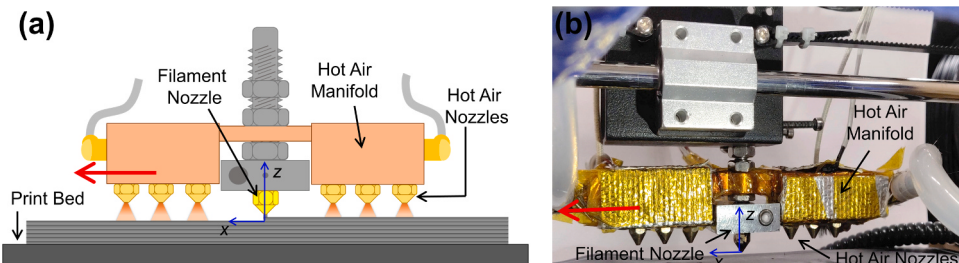


Fig. 1. (a) Schematic diagram (not to scale) and (b) picture of the air supply manifold, including hot air nozzles, that is integrated with the filament heater assembly to provide localized hot air delivery over the deposited filaments on the build platform. Red arrow indicates the direction of travel.

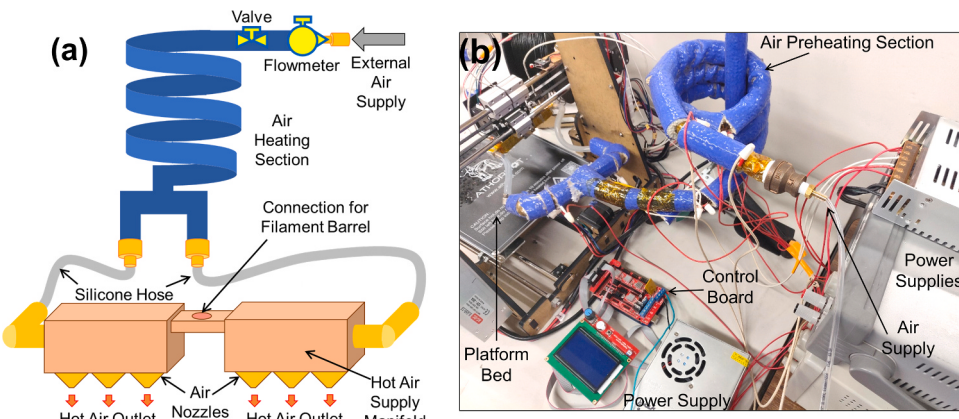


Fig. 2. (a) Schematic diagram of the hot air supply pathway (not to scale); (b) Picture of the entire experimental setup.

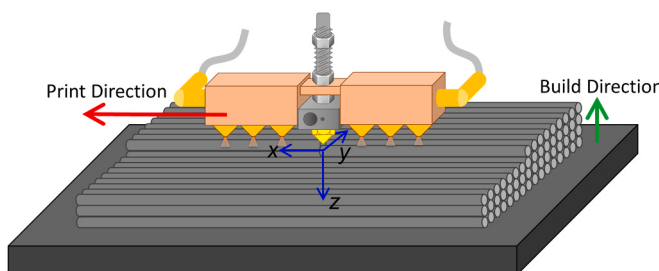


Fig. 3. Schematic of the printing process, showing the coordinate axes as well as print and build directions.

filament barrel, it is held there by two locking nuts. The manifold is covered with two layers of Kapton tape for electrical insulation and then wrapped with 24 AWG Nichrome80 wire of 5.3 Ohm/m resistance for heating. Another layer of Kapton tape is applied for additional insulation and securing the set up. One NTC thermistor is placed on the surface and the entire arrangement is covered with thermal insulation tape to minimize heat loss. Temperature of the hot air supply manifold is controlled by an Arduino Mega 2560 circuit board. It is verified through thermocouple measurements that outlet air temperature is close to the set temperature of the manifold.

The hot air supply manifold is integrated with the filament heater block and mounted on the moving head. The orientation of the manifold is controlled with a locking nut. Air is supplied from the air heating section into the manifold using two brass elbow joints and flexible silicone hose, which helps accommodate the motion of the manifold during printing. Thermal insulating tube is used over the silicone hose to minimize heat loss during operation with hot air. Due to the extended size of the air supply manifold, the raster direction zero switch is extended to avoid collision of the manifold into the 3D printer frame.

As shown in Fig. 2, the air heating section that supplies hot air into

the air supply manifold is made from copper tubing with outer and inner diameters of 15.8 mm and 12.4 mm, respectively. A total length of around 200 cm of the copper tube is bent to form a coil. The copper tubing is covered with Kapton tape for electrical insulation, wrapped with 20 AWG Nichrome80 wire and placed inside a 19 mm diameter high-temperature electrical-insulating tube sleeving.

An Alitove regulated switching power supply and an Extech DC Power Supply are used for providing the desired heating current. The air heating section is covered with a 19 mm ID high-temperature electrical-insulating tube sleeving. Air flow is regulated and measured through an Omega glass tube variable area flowmeter (model number FR2A17BVBN-OM).

2.3. Infrared (IR) thermography

A FLIR A6703sc InSb infrared camera is used for IR-based measurement of the temperature field during printing. The camera measures infrared emission in the 3.0–5.0 μm wavelength range, which is then converted into a temperature field. An emissivity value of 0.92 is used based on a calibration process reported in past work [9]. The temperature field is measured at a frame rate of 60 fps.

Once the various components of the experiments are set up and bed is leveled, temperature field is measured with the IR camera in various process conditions while printing a part of size $80 \times 12 \times 6 \text{ mm}^3$.

2.4. Cross-section characterization

Parts are printed separately for characterization of road-to-road adhesion and void fraction in the cross-section. In order to cross-section the sample without disrupting its internal details, a notch is created around the edges of one of the faces. The sample is then soaked into liquid nitrogen for about one minute and an impact load is applied on the notch. This breaks the sample clearly and reveals the cross-section [16,18]. An AmScope 3X stereo microscope with 10 MP AmScope MU

1000 digital camera is used to capture the images of the cross-section. The images are analyzed in ImageJ software to calculate the void fraction and extent of necking.

2.5. Thermal and tensile testing

Samples of 74 mm length, 36 mm width and different thicknesses (4, 8, 12, 16 mm) are printed for measurement of thermal resistance. Baseline samples are printed without hot air supply, in addition to samples printed with 200 °C air temperature at 6 liters per minute (LPM) flow rate. The print speed is 3600 mm/min. Once the samples are printed, 36 mm length is cut out from the center of the longest edge in order to produce a sample of 36 mm by 36 mm cross-section, consistent with the thermal characterization equipment. Printing of longer samples followed by cutting down to the desired size is necessitated because the impact of hot air will not be fully observable when printing a 36 mm by 36 mm sample due to the distance between the filament nozzle and hot air nozzles. The print direction in the printed samples is perpendicular to the sample thickness, over which, thermal resistance is measured. Thermal resistance of the sample is measured using a TA Instruments Fox50 equipment, which is based on the one-dimensional heat flux method [27]. The cut sample is sandwiched between two plates maintained at two different temperatures using a heater and cold water flow, respectively. The heat flow through the sample caused by the temperature difference is measured by a thin-film heat flux transducer, which is used to determine the thermal resistance of the sample.

Straight bar samples for measurement of tensile properties are printed using the experimental setup described above. The sample size is 40 mm wide by 4 mm thick by 100 mm long, based on a modified version of ASTM D3039 test standard [28]. The sample is designed to be of large width in order to ensure that the hot air nozzles are able to access the entire width of the sample during printing. The straight bar geometry also reduces the edge effect arising from the 3D layer-by-layer printing process. Such effects are commonly present in curved samples such as a dogbone. Baseline samples are printed with no hot air. In addition, samples are printed with hot air at 200 °C and 6 LPM flowrate – the parameters at which the highest void reduction is seen in cross

sections discussed later. The raster direction is perpendicular to the length of the samples, along which, tensile load is applied. All tensile tests are performed using a Shimadzu AGS-X series universal test frame with a high-precision 5 kN load cell. A stroke rate of 1 mm/min is used in stroke-controlled mode. A pair of steel grips are used to fix the specimen. Special attention is paid to avoid any slip during the tensile test. To ensure proper gripping without damaging the samples near the grip, samples are wrapped with tape near the grip area. Seven samples per sample type are tested. Data are collected in the form of load and displacement, and converted into a stress-strain diagram. Tensile properties such as ultimate tensile strength, Young's modulus and tensile toughness values are calculated. The tensile toughness is obtained by calculating the area under the stress-strain curve.

3. Results and discussion

A number of experiments are carried out to quantitatively measure the temperature field around a deposited filament due to the hot air supply and study the impact of various process parameters on the temperature field. Experiments are also carried out to measure the impact of the hot air supply on road-to-road adhesion and on thermal and mechanical properties of printed parts.

3.1. Infrared temperature measurements

Fig. 4 presents a sequence of temperature colormaps obtained from infrared thermography for the baseline case as well as a case with 200 °C air dispensing from the hot air nozzles at 6 LPM flowrate. In these colormaps, the nozzle assembly moves from right to left, and $t = 0$ corresponds to the time at which the filament nozzle is at the center of the IR camera frame, which is the point of interest for subsequent analysis. Note that the glass transition temperature of ABS is 105 °C. At the first set of colormaps at $t = -0.25$ s, the filament nozzle is barely in the frame on the right, but one of the hot air nozzles is close to the point of interest. As expected, the hot air nozzles show high temperature upwards of 200 °C for the hot air case and below 80 °C for the baseline case when there is no hot air passing through. The hot air dispensed by the hot air

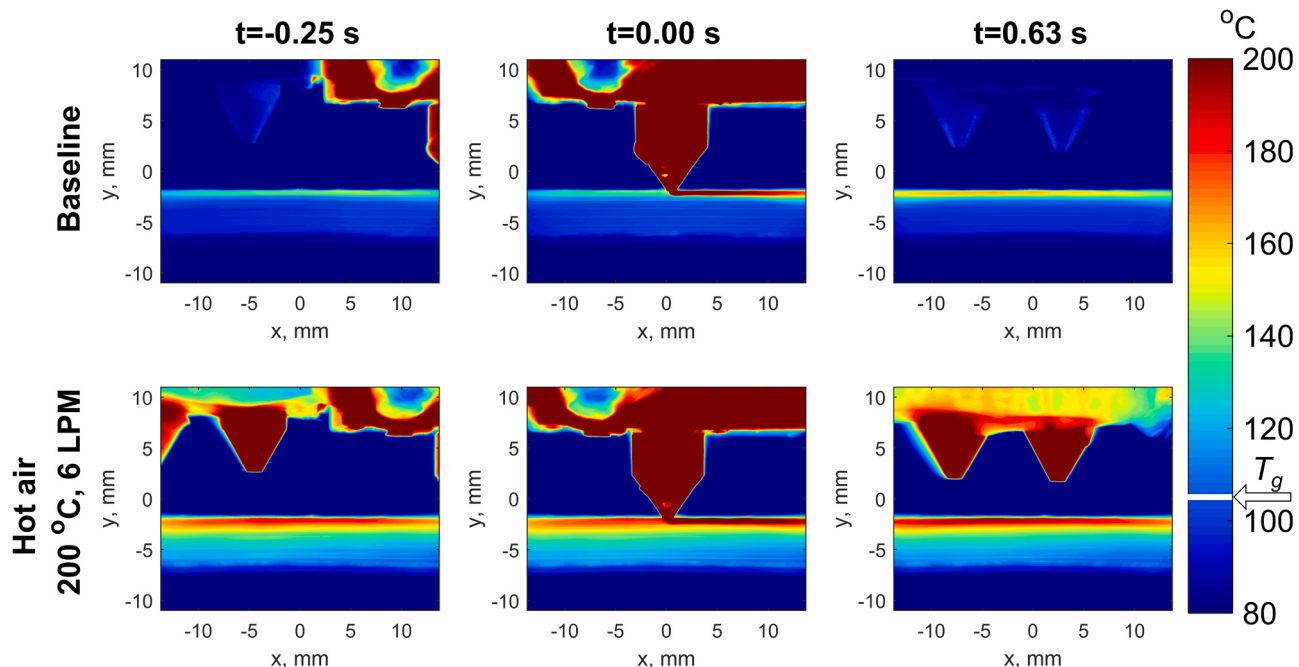


Fig. 4. Comparison of infrared-measured temperature distribution between baseline printing and printing with hot air at 200 °C and 6 LPM. Temperature colormaps are shown at three different times. In each case, the print speed is 3600 mm/min, and bed and filament nozzle temperatures are 90 °C and 230 °C, respectively. The glass transition temperature of 105 °C is indicated on the colorbar.

nozzle itself is not seen in these infrared images, since air is transparent to infrared emission. At $t = -0.25$ s, the top layer on the build platform is already 45 °C hotter in the hot air case compared to baseline. As a result, when the filament is deposited at $t = 0.0$ s, the underlying road is around 45 °C hotter in the hot air case compared to baseline. This is expected to significantly slow down the rate of cooling and ensure better road-to-road adhesion. The improved cooling rate is clearly seen in the colorplots in Fig. 4. For example, at $t = 0.63$ s, when the filament nozzle has traveled past the point of interest, the deposited filament is still 20 °C hotter in the hot air case compared to baseline. Note that the hot air nozzles seen in colorplots at $t = 0.63$ s are the ones located on the other side of the filament nozzle. The combined strategy of dispensing hot air before and after filament deposition is expected to ensure more effective road-to-road adhesion following filament deposition.

It is also seen from Fig. 4 that the thermal impact of the hot air supply may extend deeper into the previously deposited layers. Specifically, Fig. 4 shows higher temperature several mm deep into the previously deposited layers for the hot air case compared to baseline. The temperature several mm underneath the present layer is seen to be greater than the glass transition temperature for the hot air case, which indicates that hot air dispensing may promote road-to-road adhesion even in previously deposited layers underneath the present layer.

Temperature data contained in the colormaps in Fig. 4 can be extracted for quantitative comparison. This is shown and discussed in Fig. 5, where the temperature distribution along the print direction (x axis) at the interface between the top-most layer and the layer being printed is plotted for the baseline and hot air cases at three different times. In both cases, the nozzle assembly moves from right to left. In the hot air case, air at 200 °C is dispensed at 6 LPM flowrate. At $t = -0.25$ s, the filament dispensing nozzle is still far from the center of the frame, $x = 0$, but the temperature distribution is already significantly elevated for the hot air case compared to baseline (blue curves) due to the hot air dispensed by the nozzles that have already traveled past the point of interest. This preheating prior to filament deposition is expected to promote adhesion of the deposited filament with those already deposited previously. At $t = 0.0$ s, the filament-dispensing nozzle reaches the center of the frame, resulting in a steep temperature rise for both cases (red curves). Some residual effect of the hot air supply is still seen at $t = 0$, particularly prior to $x = 0$. Finally, at $t = 0.63$ s, the temperature cools off, but the rate of cooldown is much lower for the hot air case than baseline (green curves). In fact, to the left of the point of interest, i.e., prior to $x = 0$, temperature actually increases. This is because by now, the trailing set of hot air nozzles are dispensing hot air over the recently printed filament. On the overall, the deposited filament spends much longer time above glass transition temperature compared to the baseline case, which is expected to improve the bond quality and enhance the properties of the printed part.

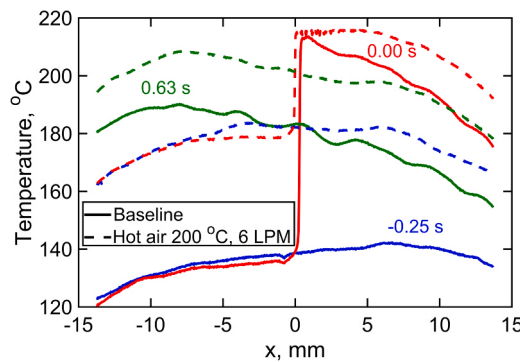


Fig. 5. Comparison of measured temperature along the print direction between baseline and hot air cases (200 °C at 6 LPM) at three different times corresponding to Fig. 4. In each case, the print speed is 3600 mm/min, and bed and filament nozzle temperatures are 90 °C and 230 °C, respectively.

Fig. 6 presents the impact of the hot air dispensing on temperature distribution in previously-deposited layers. This Figure compares the measured temperature as a function of depth, z , at three different times for the baseline case and the case with hot air dispensed at 200 °C and 6 LPM. Note that $z = 0$ corresponds to the top of the newly deposited filament, which is why, the curves at $t = -0.25$ s (prior to filament deposition) do not extend all the way to $z = 0$. Fig. 6 shows that the thermal impact of the dispensed hot air is experienced not just at $z = 0$, but also several mm deep. The temperature curves for the hot air are higher than the baseline case. For the baseline case, the temperature curve close to $z = 0$ shoots up at $t = 0$ due to new filament deposition, and is much lower at other times. On the other hand, the curves for the hot air case are at all times elevated compared to the baseline case. This is directly attributable to the high temperature micro-environment around the filament due to the hot air, which reduces heat loss and maintains higher temperature several mm deep into previously deposited layers.

The improved thermal history of a polymer road represented in Fig. 6 is expected to play a key role in road-to-road adhesion. The longer the interface temperature stays above glass transition temperature, the greater is the extent of reptation and entanglement of polymer chains across the interface [4], and therefore, greater is the degree of adhesion between roads.

Note that the sample size plays a key role in determining the depth to which the thermal impact of the hot air is experienced. Large samples with relatively large surface area are likely to cool down faster, and therefore, in that case, it may be necessary to increase the hot air flow rate or the number of hot air nozzles to compensate for the cooling effect.

3.2. Effect of process parameters

Hot air temperature is a key parameter associated with the hot air dispensing process. The impact of hot air temperature on the resulting temperature distribution around the filament is important to quantify, in order to fully understand how the bond quality is impacted by this parameter. Towards this, a number of measurements are carried out, in which, air is dispensed at several different temperatures while keeping the flowrate constant at 6 LPM. The resulting temperature at one point is plotted as a function of time in Fig. 7. The baseline case, with no hot air dispensed, is also shown. These curves characterize the rate of cooling down of the filament following the deposition process. In each case, Fig. 7 shows that the filament cools down starting at $t = 0$ s, as the nozzle assembly moves away. Fig. 7 shows that, compared to the baseline case, the filament temperature is elevated significantly – and the cooling process is slowed down considerably – by the hot air. In general, the greater the hot air temperature, the more elevated is the filament temperature, as expected. There are practical limits to this, however,

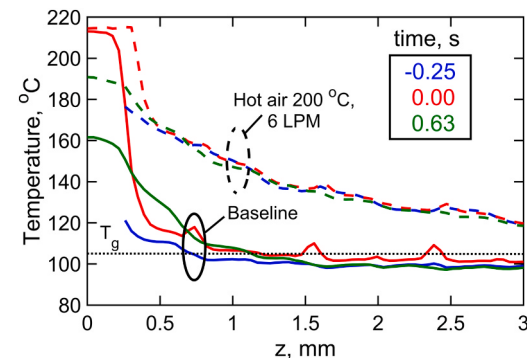


Fig. 6. Comparison of measured temperature as a function of z between baseline and hot air cases (200 °C at 6 LPM) at three different times. The glass transition temperature is indicated by a dashed line across the plot.

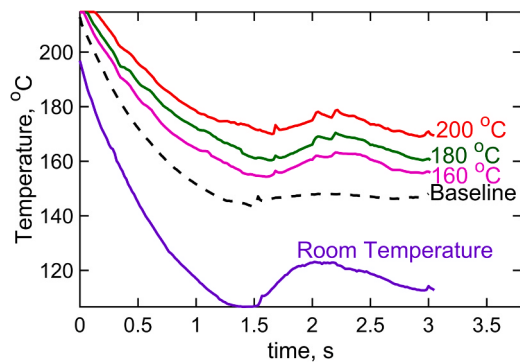


Fig. 7. Temperature as a function of time at a fixed point following filament deposition for different hot air temperatures. Data for baseline case with no hot air are also shown for comparison. The air flow rate is 6 LPM in each case.

because if the dispensed air is too hot, it may degrade and damage the top surface of the deposited filament. A temperature curve is also measured and plotted in Fig. 7 for a contrasting case where the hot air nozzle dispenses unheated air at room temperature. This is expected to quench and rapidly cool down the filament, resulting in poor bond quality. This is clearly seen in the bottom-most curve in Fig. 7. These data further establish the case that dispensing hot air slows down filament cooling, which is expected to improve adhesion. These data also show, as expected, that dispensing room temperature air is not useful, and, in fact, has an undesirable effect on filament bonding.

Note that the cooling curves shown in Fig. 7 do not go down to the bed temperature because at around $t = 1.6$ s, the nozzle assembly returns to print the next filament. Fig. 7 shows that in the baseline case, the temperature plateaus out, whereas when hot air is dispensed, it results in a rise in temperature. This is because of hot air being dispensed by nozzles that have returned along with the filament nozzle to print the next line. The small bump in the baseline case around the same time is likely due to heat transfer directly from the hot filament nozzle. In the room temperature air case, the plateau occurs because the filament has cooled down dramatically due to the quenching effect of the cold air, which then heats back up slightly due to the deposition of the second filament.

3.3. Characterization of road-to-road adhesion and thermal/mechanical properties

The neck size between roads is representative of the quality of road-to-road adhesion, since polymer chain reptation across the interface at high temperature increases the neck size [6]. The impact of the elevated temperature distribution due to hot air dispensing on necking and adhesion between roads is investigated next. Representative samples are printed for the baseline case as well as several cases of hot air dispense. Cross-section images of these samples are obtained, as described in Section 2.4, and presented in Fig. 8. The baseline cross-section is shown in Fig. 8(a) and shows minimal necking between filaments, both inter-layer and intra-layer. Fig. 8(b) shows the cross-section for hot air at 200 °C and 6 LPM – the optimal case amongst the ones investigated in this work. Significant improvement in neck size between roads can be seen visually in this case compared to the baseline. The neck sizes in Fig. 8(a) and (b) are measured using image analysis. It is found that the average neck size increases from 0.14 mm in the baseline case (Fig. 8(a)) to 0.26 mm in the case of hot air at 200 °C and 6 LPM (Fig. 8(b)). This improvement is attributable to increased effectiveness of road-to-road bonding – both in-layer and between layers – due to the elevated temperature and increased cool down time, as shown in temperature measurements in Fig. 5. The improvement in neck size reported here is comparable to results from post-process annealing [18]. Compared to the long time taken for post-process annealing and the associated risk of warping, similar improvement in neck size is obtained in the present work in a more seamless, *in situ* fashion.

In addition to improved neck size, an estimate of the void fraction carried out by measuring the fraction of dark area in a representative square region shows that the void fraction reduces from 11.9% in the baseline case (Fig. 8(a)) to 4.0% in the hot air case at 200 °C and 6 LPM (Fig. 8(b)).

Cross-sections are also carried out at two other process conditions. When the hot air is dispensed at the same temperature but greater flowrate (12 LPM), the improvement in void fraction is marginal, as shown in Fig. 8(c). Finally, when room temperature air is dispensed at 12 LPM, it is expected to have a negative impact on the bond quality due to rapid cool down of the filaments. The resulting cross section, shown in Fig. 8(d), is consistent with this expectation, and shows very poor bonding between filaments. The poor performance of the room temperature air case also establishes that the improvement in filament adhesion observed in this work is primarily a thermal effect, caused by the slowing down of the cooling curve, rather than due to any

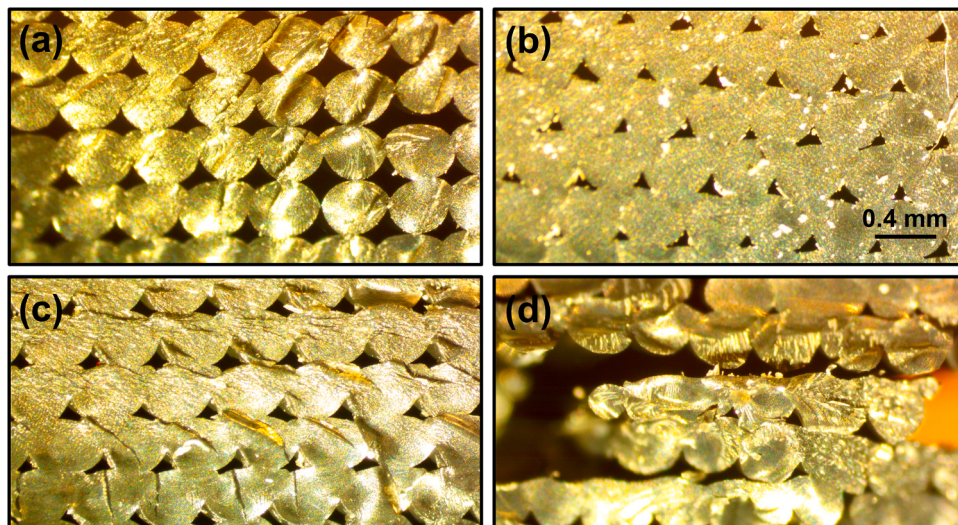


Fig. 8. Comparison of cross-section images of printed samples for four cases – (a) baseline (no air), (b) hot air at 200 °C, 6 LPM, (c) hot air at 200 °C, 12 LPM, (d) air at room temperature, 12 LPM.

mechanical compression of the filament by the impinging jet.

Two sets of measurements are carried out to understand the impact of hot air dispensing on the thermal and mechanical properties of printed parts.

As described in [Section 2.5](#), test samples of different thicknesses are printed for the baseline and improved process with hot air at 200 °C and 6 LPM. Thermal resistance measurements of these samples are carried out using the one-dimensional heat flux method. Thermal resistance as a function of thickness is plotted for the two cases in [Fig. 9](#). These data show reduced thermal resistance for the hot air samples compared to baseline at each thickness. In both cases, the thermal resistance increases with increasing thickness, as expected, but at a lower rate for the hot air sample compared to baseline. Both curves are linear, with R^2 values exceeding 0.99 in both cases, which confirms the validity of the thermal resistance measurement. The slope of the linear curves provides a value of thermal conductivity of the samples. Data in [Fig. 9](#) indicate a 35% improvement in thermal conductivity for the hot air case (0.132 W/mK) compared to baseline (0.098 W/mK). This is consistent with the improved voiding shown in [Fig. 8](#), as well as the increased time to cool down shown by temperature measurements in [Fig. 6](#).

In addition to thermal resistance measurements, uniaxial tensile testing of printed samples is also carried out. The printing and tensile testing of samples is described in [Section 2.5](#). A total of seven samples are prepared such as that the load direction is normal to the direction of the raster orientation, which helps investigate the impact of hot air on interfacial adhesion between polymer roads. [Fig. 10](#) shows the stress-strain diagram for the baseline case with no hot air, and the case with hot air at 200 °C for one sample of each type. Data for other replicates are very similar. [Table 1](#) summarizes the values of key mechanical properties obtained from the tensile test data, including standard deviation.

[Fig. 10](#) shows about 19% improvement in Ultimate Tensile Stress (UTS) and 145% improvement in the tensile toughness of samples printed with hot air compared to the baseline case. The key contributor of the significant improvement in toughness is the softening of the samples with hot air. The strain to failure of the baseline sample is about 3% whereas the strain to failure of the heat treated sample is more than 6.25%. A distinct shift in the stress-strain response is noticed at around 0.75% strain where the baseline curve becomes significantly steeper than that of the sample printed with hot air. Such a trend in the stress-strain curve is associated with material softening. In other words, the degree of ductility of the sample printed with hot air is distinctly higher than the baseline sample, which, in turn, is responsible for increased strain-to-failure and toughness. Note that the direction of loading is normal to the interfacial contact between the polymer roads.

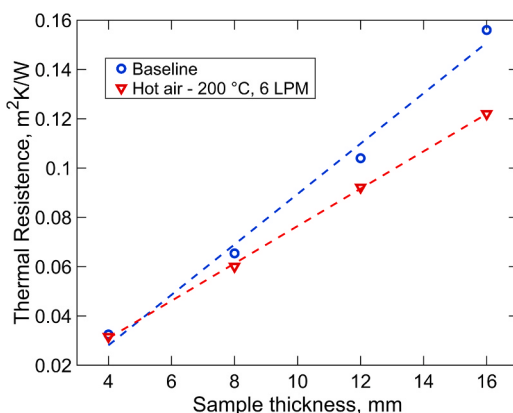


Fig. 9. Measured thermal resistance as a function of sample thickness for baseline and improved samples subjected to hot air at 200 °C temperature and 6 LPM flowrate. Slopes of these data correspond to thermal conductivity of the samples.

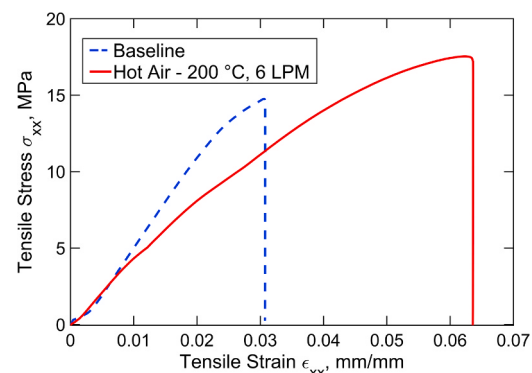


Fig. 10. Stress-strain curves for baseline and improved samples subjected to hot air at 200 °C temperature and 6 LPM flowrate.

As such, the deformation process of the printed samples is governed by the change in interfacial contacts and polymer configurations due to applied heat. Presence of the hot air also reduces and rearranges the void geometry and formation, as is clearly evident from a comparison of cross-sections of baseline and hot air samples in [Fig. 8\(a\)](#) and (b), respectively. Both factors are likely to have contributed in improving the ultimate tensile strength and toughness of the hot air samples.

Note that since the focus of the present work is to investigate how hot air helps improve road-to-road adhesion, all thermal/mechanical characterization described above is carried out with the load being applied normal to the raster direction. Note that the gap between the filament nozzle and hot air nozzle must be small enough to ensure that the entire width of the sample being printed is exposed to the hot air impingement. This is the reason why thermal and tensile test samples printed in this work are of somewhat large size.

3.4. Process mechanisms related to localized hot air supply

This section briefly discusses key process mechanisms related to localized hot air supply and its impact on the just-deposited filament. This process is likely to involve three distinct mechanisms. The first one relates to direct heating of the filament by the impinging hot air. The second and third mechanisms relate to convective heat transfer from the filament to air in its vicinity. On one hand, the impinging hot air may raise the air temperature in the vicinity of the filament, which slows down the rate of cooling of the filament. On the other hand, the impinging hot air may also increase the convective heat transfer coefficient due to the additional fluid flow caused around the filament, which is undesirable since it may increase the rate of convective heat loss. Due to the relatively low flow speeds (less than 0.1 m/s), the third mechanism is likely to be weaker than the other two since the convective heat transfer coefficient scales with the flow speed. Therefore, it is likely that, on the overall, hot air impingement results in reduced convective heat loss from the filament, and therefore, increased time at elevated temperature. This is expected to result in improved filament-to-filament adhesion and improved tensile properties as experimentally observed in this work. For extremely high flow speeds, the increase in convective heat transfer coefficient may dominate, but such flow speeds are anyway unlikely to be practical for 3D printing.

In addition to the thermal mechanisms outlined above, the impinging hot air jet may also apply direct compressive force on the filament. However, due to the relatively low density of air, particularly at high temperatures, this is likely to be a negligible effect. Experimental data shown in [Fig. 8\(d\)](#) is consistent with this hypothesis.

The key process parameters that govern these heat transfer processes include the temperature and flow rate of the hot air supply, both of which have been investigated experimentally in this work. In addition, the key geometrical parameters in this problem include the nozzle-to-

Table 1

Comparison of Tensile test properties of baseline samples with those printed with 6 LPM hot air flow at 200 °C.

Sample description	Ultimate strength (MPa)		Increase in ultimate tensile strength, %	Tensile Toughness (MJ/m ³)		Increase in tensile toughness, %
	Mean	Standard deviation		Mean	Standard deviation	
No hot air (Baseline)	14.8	2.7	–	0.23	0.12	–
Hot air at 6 LPM and 200 °C	17.5	1.6	18.8%	0.56	0.11	145.8%

platform gap, the distance between air and filament nozzles and the orientation of the air nozzle relative to the build platform. Numerical simulations, for example, based on Computational Fluid Dynamics (CFD) may be an important direction of future work to supplement the experimental results presented here. Such simulations may help better understand these process mechanisms and the impact of various process parameters on the filament.

4. Conclusions

This work demonstrates that the hot air dispensing technique results in significant improvement in void formation and thermal/mechanical properties of the printed parts. Compared to other methods to supply thermal energy to the deposited filament through laser, IR lamp and other energy sources [20–24], the present approach is simpler, lower cost and easier to integrate with the filament nozzle assembly. For example, in the present approach, there is no need for complicated optical alignment, as is the case with laser-based heating [22]. There is minimal capital cost in hot air dispensing compared to the cost of laser/IR/microwave energy sources and the associated optical components. The energy consumption for producing hot air is also quite low (estimated to be around 17W for 6 LPM air at 200 °C) compared to other energy sources.

Several geometrical parameters related to the hot air nozzles presented in this work are largely unoptimized, and optimization in the future through experiments and/or numerical simulations may result in further process improvement. For example, the gap between the filament nozzle and the hot air nozzles is fixed in the experiments described here. Reduction of this gap may further improve filament adhesion, particularly for small-sized parts. The impact of other changes, such as the orientation of the hot air nozzles could also be studied in the future. Finally, the present experiments are carried out on relatively small-sized parts. In order to implement this technique for big area additive manufacturing, the greater rate of heat loss may need to be compensated by increasing the flow rate of hot air or increasing the number of hot air nozzles. Further, for big area additive manufacturing, the length of hot air tubes may need to be increased to accommodate the larger range of the print head. In an extreme case, when the print size is extremely large, it may be possible to mount the air heater on the print head itself, thereby completely eliminating the need for tubing at all.

CRediT authorship contribution statement

H. Prajapati: Methodology, Investigation, Visualization, Data Curation. **S. Salvi:** Methodology, Investigation, Visualization, Data Curation. **D. Ravoori:** Investigation, Visualization. **M. Qasaimeh:** Investigation. **A. Adnan:** Methodology, Supervision. **A. Jain:** Conceptualization, Methodology, Supervision, Project Administration. All authors contributed towards Writing Original Draft, Review and Editing.

Data Availability Statement

The raw/processed data required to reproduce these findings cannot be shared at this time as the data also forms part of an ongoing study.

Declaration of Competing Interest

The authors declare that they have no known competing financial interests or personal relationships that could have appeared to influence the work reported in this paper.

Acknowledgement

The authors would like to gratefully acknowledge helpful discussions with Professor Frank Lu.

References

- [1] D. Dimitrov, K. Schreve, N. de Beer, Advances in three dimensional printing – state of the art and future perspectives, *Rapid Prototyp. J.* 12 (2006) 136–147.
- [2] D. Ravoori, C. Lowery, H. Prajapati, A. Jain, Experimental and theoretical investigation of heat transfer in platform bed during polymer extrusion based additive manufacturing, *Polym. Test.* 73 (2019) 439–446.
- [3] S.F. Costa, F.M. Duarte, J.A. Covas, Estimation of filament temperature and adhesion development in fused deposition techniques, *J. Mater. Process. Technol.* 245 (2017) 167–179.
- [4] F. Yang, R. Pitchumani, Healing of thermoplastic polymers at an interface under nonisothermal conditions, *Macromolecules* 35 (2002) 3213–3224.
- [5] O. Pokluda, C.T. Bellehumeur, J. Vlachopoulos, Modification of Frenkel's model for sintering, *AIChE J.* 43 (1997) 3253–3256.
- [6] C. Bellehumeur, L. Li, Q. Sun, P. Gu, Modeling of bond formation between polymer filaments in the fused deposition modeling process, *J. Manuf. Process* 6 (2004) 170–178.
- [7] J.E. Seppala, K.D. Migler, Infrared thermography of welding zones produced by polymer extrusion additive manufacturing, *Addit. Manuf.* 12 (2016) 71–76.
- [8] J.F. Rodriguez, J.P. Thomas, J.E. Renaud, Characterization of the mesostructure of fused-deposition acrylonitrile-butadiene-styrene materials, *Rapid Prototyp. J.* 6 (2000) 175–185.
- [9] H. Prajapati, D. Ravoori, A. Jain, Measurement and modeling of filament temperature distribution in the standoff gap between nozzle and bed in polymer-based additive manufacturing, *Addit. Manuf.* 24 (2018) 224–231.
- [10] A. D'Amico, A.M. Peterson, An adaptable FEA simulation of material extrusion additive manufacturing heat transfer in 3D, *Addit. Manuf.* 21 (2017) 422–430.
- [11] A. Lepoirre, N. Boyard, A. Levy, V. Sobotka, Heat transfer and adhesion study for the FFF additive manufacturing process, *Procedia Manuf.* 47 (2020) 948–955.
- [12] E. Ferraris, J. Zhang, B. Van Hooreweder, Thermography based in-process monitoring of fused filament fabrication of polymeric parts, *CRP Ann.* 68 (2019) 213–216.
- [13] K. Choo, B. Friedrich, T. Daugherty, A. Schmidt, C. Patterson, M.A. Abraham, B. Conner, K. Rogers, P. Cortes, E. MacDonald, Heat retention modeling of large area additive manufacturing, *Addit. Manuf.* 28 (2019) 325–332.
- [14] J. Go, A.J. Hart, Fast desktop-scale extrusion additive manufacturing, *Addit. Manuf.* 18 (2017) 276–284.
- [15] D.D. Phan, Z.R. Swain, M.E. Mackay, Rheological and heat transfer effects in fused filament fabrication, *J. Rheol.* 62 (2018) 1097–1107.
- [16] D. Ravoori, H. Prajapati, V. Tallurati, A. Adnan, A. Jain, Nozzle-integrated pre-deposition and post-deposition heating of previously deposited layers in polymer extrusion based additive manufacturing, *Addit. Manuf.* 28 (2019) 719–726.
- [17] J. Go, A.J. Hart, Fast desktop-scale extrusion additive manufacturing, *Addit. Manuf.* 18 (2017) 276–284.
- [18] H. Prajapati, D. Chalise, D. Ravoori, R.M. Taylor, A. Jain, Improvement in build-direction thermal conductivity in extrusion-based polymer additive manufacturing through thermal annealing, *Addit. Manuf.* 26 (2019) 242–249.
- [19] K.R. Hart, R.M. Dunn, J.M. Sietins, C.M.H. Mock, M.E. Mackay, E.D. Wetzel, Increased fracture toughness of additively manufactured amorphous thermoplastics via thermal annealing, *Polymer* 144 (2018) 192–204.
- [20] V. Kishore, C. Ajinjeru, A. Nycz, B. Post, J. Lindahl, V. Kunc, C. Duty, Infrared preheating to improve interlayer strength of big area additive manufacturing (BAAM) components, *Addit. Manuf.* 14 (2017) 7–12.
- [21] A. Nycz, V. Kishore, J. Lindahl, C. Duty, C. Carnal, V. Kunc, Controlling substrate temperature with infrared heating to improve mechanical properties of large-scale printed parts, *Addit. Manuf.* 33 (2020), 101068.
- [22] A.K. Ravi, A. Deshpande, K.H. Hsu, An in-process laser localized pre-deposition heating approach to inter-layer bond strengthening in extrusion based polymer additive manufacturing, *J. Manuf. Process.* 24 (2016) 179–185.

- [23] C.B. Sweeney, B.A. Lackey, M.J. Pospisil, T.C. Achee, V.K. Hicks, A.G. Moran, B. R. Teipel, M.A. Saed, M.J. Green, Welding of 3D-printed carbon nanotube–polymer composites by locally induced microwave heating, *Sci. Adv.* 3 (2017), e1700262.
- [24] C. Zawaski, C. Williams, Design of a low-cost, high-temperature inverted build environment to enable desktop-scale additive manufacturing of performance polymers, *Addit. Manuf.* 33 (2020), 101111.
- [25] S. Partain, Fused deposition modeling with localized pre-deposition heating using forced air, M.S. Thesis, Montana State University, 2007.
- [26] M. Adel, O. Abdelaal, A. Gad, A.B. Nasr, A.M. Khalil, Polishing of fused deposition modeling products by hot air jet: evaluation of surface roughness, *J. Mater. Proc. Technol.* 251 (2018) 73–82.
- [27] H. Prajapati, D. Ravoori, R. Woods, A. Jain, Measurement of anisotropic thermal conductivity and inter-layer thermal contact resistance in polymer Fused Deposition Modeling (FDM), *Addit. Manuf.* 21 (2018) 84–90.
- [28] Standard Test Method for Tensile Properties of Polymer Matrix Composite Materials, ASTM International, available at (<https://www.astm.org/Standards/D3039>), accessed 08/14/2020.